

Investigating the convergence properties of iterative ptychography for atomic-resolution low-dose imaging

Tamazouzt Chennit^{a,b,*}, Songge Li^{a,b}, Hoelen L. Lalandec Robert^{a,b}, Christoph Hofer^{a,b}, Nadine J. Schrenker^{a,b}, Liberato Manna^c, Sara Bals^{a,b}, Timothy J. Pennycook^{a,b}, Jo Verbeeck^{a,b}

^aEMAT, University of Antwerp, Groenenborgerlaan 171, 2020 Antwerp, Belgium

^bNANOLight Center of Excellence, University of Antwerp, Groenenborgerlaan 171, 2020 Antwerp, Belgium

^cDepartment of Nanochemistry, Istituto Italiano di Tecnologia (IIT), 16163 Genova, Italy

Abstract

This study investigates the convergence properties of a collection of iterative electron ptychography methods, under low electron doses ($< 10^3 e^-/\text{\AA}^2$) and gives particular attention to the impact of the user-defined update strengths. We demonstrate that carefully chosen values for this parameter, ideally smaller than those conventionally met in the literature, are essential for achieving accurate reconstructions of the projected electrostatic potential. Using a 4D dataset of a thin hybrid organic-inorganic formamidinium lead bromide (FAPbBr₃) sample, we show that convergence is in practice achievable only when the update strengths for both the object and probe are relatively small compared to what is found in literature. Additionally we demonstrate that under low electron doses, the reconstructions initial error increases when the update strength coefficients are reduced below a certain threshold emphasizing the existence of critical values beyond which the algorithms are trapped in local minima. These findings highlight the need for carefully optimized reconstruction parameters in iterative ptychography, especially when working with low electron doses, ensuring both effective convergence and correctness of the result.

Keywords: Electron Ptychography, Low-dose Imaging, Beam-sensitive Materials, 4D-STEM, Iterative Ptychography Methods

1. Introduction

Atomic resolution imaging of crystalline materials, typically requiring high electron doses [1], has become a routine procedure in transmission electron microscopy (TEM) [2], in particular, thanks to the widespread use of aberration correction [3]. However, numerous specimens of interest are susceptible to beam damage, which makes high-resolution challenging [4]. As described e.g. in references [5–7], two damage mechanisms are prevalent in TEM. Those are radiolysis and knock-on displacement. Radiolysis primarily affects semiconductors and insulators, and results from the inelastic interaction between the electron beam and core electrons in the specimen, i.e. leading to ionization. Knock-on effects are typically more dominant in metals and result from elastic interactions, involving significant energy transfers to atoms and their displacement. This damage mechanism is particularly common in two-dimensional materials, where it often manifests as hole formation [8, 9].

Inorganic perovskites such as CsPbI₃ [10, 11], hybrid organic-inorganic perovskites such as methylammonium lead iodide (MAPBI₃) [12] or formamidinium lead bromide

(FAPbBr₃) [13], zeolites [14–16] and metal-organic frameworks (MOF) [17–20] are prominent examples of beam-sensitive materials in the materials science domain. Moreover, dose-sensitivity is of significant importance in biological sciences [21, 22], especially when imaging proteins [23] and viruses [24].

Conventional TEM (CTEM) is widely used for low-dose imaging; however, methods based on scanning TEM (STEM), such as the integrated center of mass (iCoM) [15, 25–27] and ptychography, have been used and have shown promising capacities as well [10, 24, 28–35].

Ptychography, belonging to the family of coherent diffractive imaging (CDI) techniques [36–40], was initially introduced by Hoppe et al. [41–43] in 1969. Recently, there has been renewed interest in ptychographic methods that employ fast electrons, particularly with the advent of direct electron detectors (DED) [44–51]. These detectors, having frame rates of typically 10^3 to 10^4 per second, permit the acquisition of four-dimensional STEM (4D-STEM) datasets [52] with reasonable recording times, as required in ptychography, though with stability and scan size restrictions. Those last remaining limits were largely removed in the last few years, following the introduction of event-driven detectors [53, 54] enabling sub-microsecond dwell times in STEM [55–57] and facilitating low-dose acquisitions. With those experimental improvements, pty-

*Corresponding author: tamazouzt.chennit@uantwerpen.be

chography was thus enabled as a powerful phase retrieval technique permitting atomic resolution with high dose efficiency.

Ptychography includes analytical approaches such as the Wigner distribution deconvolution (WDD) [58–60] and single-sideband (SSB) [52, 61, 62] methods, originating in the 1990s. An iterative variant was later introduced in the form of the ptychographic iterative engine (PIE) [63, 64] which was furthermore extended to simultaneously refine both the object and the illumination, resulting in the extended version of PIE known as ePIE [65, 66]. Other methods, such as error reduction (ER) [37, 67, 68] and weighted average sequential projection (WASP) [69], have also been proven to be efficient. Iterative methods involve repeatedly updating both the specimen and the probe functions, with each update weighted by a user-defined update coefficient or strength.

To date, only a few studies have explored the impact of these update coefficients across a range of iterative algorithms. One notable example is [66], which compares various ePIE-like algorithms. However, that study was not specifically aimed at achieving atomic resolution, nor did it address the challenges associated with low electron doses. In this manuscript, we fill this gap by investigating the convergence behavior of these iterative methods under low electron dose conditions, with a particular focus on how the choice of update strengths influences their performance. Using both simulated and experimental 4D datasets from a FAPbBr₃ nanocrystal, we show that the convergence dynamics of ePIE-like algorithms are influenced not only by acquisition parameters such as electron dose but also by external factors like the update coefficients. Our findings indicate that the performance generally degrades beyond a certain threshold of update coefficients, suggesting that these iterative algorithms are sensitive to such external parameters. Moreover, we find that the regularized version of ePIE (rPIE) demonstrates greater robustness and more stable convergence across a range of update strengths compared to the standard ePIE algorithm.

The first section of this manuscript explores the fundamental principles of both analytical and iterative approaches to ptychography, while the second section provides a comparative evaluation of these techniques against the direct SSB solution and finally, the core of the manuscript is devoted to examining how the user-defined update coefficients affect both the quality of the reconstructions and the convergence behavior of the algorithms, especially under low electron dose conditions.

2. Fundamental aspects of electron ptychography

2.1. The phase problem

In a conventional 4D-STEM experiment, a well-focused electron probe is scanned over the sample and a convergent electron beam diffraction (CBED) pattern is recorded

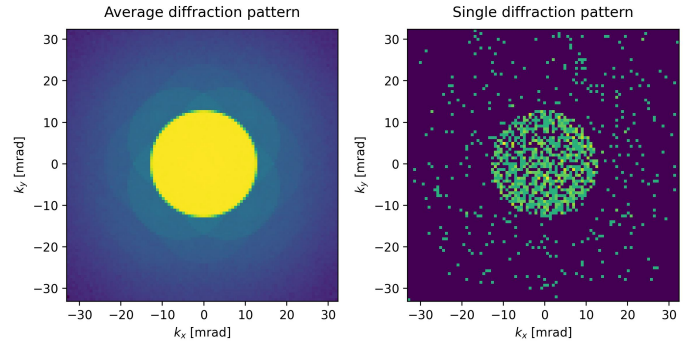


Figure 1: Position-averaged CBED (to the left) and single CBED (to the right) obtained from a simulated 4D dataset of 2.5 nm thick FAPbBr₃ using a maximum collection angle of 32 mrad, a convergence angle of 13 mrad, an acceleration voltage of 200 kV. The probe is aberration-free.

in the far-field by a DED. Figure 1 represents a simulated single CBED pattern and its scan position-averaged counterpart, obtained with a maximum collection angle of 32 mrad using a low electron count dataset showing Poisson counting noise.

The recorded intensity in the far-field is given by:

$$\begin{aligned} I_{\text{CBED}}(\mathbf{K}_r, \mathbf{R}_0) &= \left| \tilde{\psi}(\mathbf{K}_r, \mathbf{R}_0) \right|^2 \\ &= \left| \mathcal{F}[\psi(\mathbf{r}, \mathbf{R}_0)] \right|^2 \\ &= \left| \mathcal{F}[P(\mathbf{r} - \mathbf{R}_0) O(\mathbf{r})] \right|^2 \end{aligned} \quad (1)$$

In such an experiment, the measurable intensity $I_{\text{CBED}}(\mathbf{K}_r, \mathbf{R}_0)$ given by equation 1 corresponds to the squared modulus of the Fourier transform of the real-space exit wave. For a relatively thin specimen, where the phase object approximation (POA) holds, as utilized e.g. in ref. [58, 64, 65, 70], this exit wave can be expressed as the product of the object function $O(\mathbf{r})$ with the scanned probe $P(\mathbf{r} - \mathbf{R}_0)$. Here \mathbf{R}_0 denotes the relative shift between the probe’s position and the object and \mathbf{r} denotes the coordinate vector in the real space. This can be formally written as:

$$\psi(\mathbf{r}, \mathbf{R}_0) = O(\mathbf{r}) P(\mathbf{r} - \mathbf{R}_0) \quad (2)$$

Here, \mathbf{K}_r denotes the reciprocal space coordinate vector, $\psi(\mathbf{r}, \mathbf{R}_0)$ and $\tilde{\psi}(\mathbf{K}_r, \mathbf{R}_0)$ are the exit wave at the specimen plane and its far-field projection, respectively.

As the recording consists of Poisson-distributed electron counts [71, 72] determined by the squared modulus of $\tilde{\psi}(\mathbf{K}_r, \mathbf{R}_0)$, the phase distribution of the far-field wave is not directly accessible. As a consequence, the spatially dependent, interaction-induced, phase shift experienced locally by the electron probe cannot be recovered from a single CBED pattern, except in limited conditions [39, 73, 74]. This is often referred to as the “*phase problem*” [75] in optics and electron microscopy and presents a significant challenge, particularly when imaging at low

electron doses, as the recorded intensities may be insufficient for unambiguous interpretation using conventional STEM methods.

Continuing, the specimen transmission function $O(\mathbf{r})$ is given by:

$$O(\mathbf{r}) = M(\mathbf{r}) \exp(-i\theta(\mathbf{r})) \quad (3)$$

Here, $\theta(\mathbf{r})$ represents the phase shift induced by the interaction with the specimen and $M(\mathbf{r})$ is an amplitude modulation term. Under the POA, it is postulated that the specimen induces changes to the incident electron wave solely in phase. Consequently, $M(\mathbf{r})$ can be assigned a constant value of 1, although in practice a lack of perfect coherence or the POA not being perfectly fulfilled will lead to a non-unitary amplitude in the result. The integration of the phase shift along the specimen's thickness yields a relationship between $\theta(\mathbf{r})$ and the projected electrostatic potential of the specimen $V_t(\mathbf{r})$ given by:

$$O(\mathbf{r}) = \exp(i\sigma V_t(\mathbf{r})) \quad (4)$$

The quantity σ then represents the interaction coefficient.

When the imaged object is sufficiently light in addition to being thin, such that the range of values covered by $\sigma V_t(\mathbf{r})$ is negligible compared to 1, the exponent in the object transmission function can be Taylor-expanded to the first-order. Consequently, $O(\mathbf{r})$ becomes linearly dependent on the projected potential. This approximation is referred to as the weak phase object approximation (WPOA).

2.2. Single sideband (SSB)

The extraction of the phase of the object's transmission function in the framework of the single sideband (SSB) algorithm, as initially described by Rodenburg et al. [61] and later tested for atomic resolution imaging [29, 62, 76], involves the calculation of the Fourier transform of the recorded intensity $|\tilde{\psi}(\mathbf{K}_r, \mathbf{R}_0)|^2$ with respect to the probe position \mathbf{R}_0 . This can be written as:

$$G(\mathbf{K}_r, \mathbf{Q}_0) = \int |\tilde{\psi}(\mathbf{K}_r, \mathbf{R}_0)|^2 \exp(-2i\pi\mathbf{R}_0\mathbf{Q}_0) d\mathbf{R}_0 \quad (5)$$

Under the WPOA, $G(\mathbf{K}_r, \mathbf{Q}_0)$ is equal to:

$$\begin{aligned} G(\mathbf{K}_r, \mathbf{Q}_0) &= |A(\mathbf{K}_r)|^2 \delta(\mathbf{Q}_0) \\ &+ A(\mathbf{K}_r) A^*(\mathbf{K}_r + \mathbf{Q}_0) i\tilde{\theta}(\mathbf{Q}_0) \\ &- A^*(\mathbf{K}_r) A(\mathbf{K}_r - \mathbf{Q}_0) i\tilde{\theta}(\mathbf{Q}_0) \end{aligned} \quad (6)$$

Here, $A(\mathbf{K}_r)$ denotes the aperture function, which comprises both an amplitude and an aberration function $\chi(\mathbf{K}_r)$ and $\tilde{\theta}$ represents the Fourier transform of the phase shift.

$$\begin{aligned} A(\mathbf{K}_r) &= \Omega \exp(i\chi(\mathbf{K}_r)) \\ \Omega &= 1 \quad \text{inside the aperture} \\ \Omega &= 0 \quad \text{outside the aperture} \end{aligned} \quad (7)$$

In the triple overlap region where the 0th order scattered disk and the first-order scattered disks overlap, the two last terms cancel out. As a result, this area cannot contribute to the retrieval of the spatially dependent phase shift. It is thus only achievable by exploitation of the double overlap region, between the 0th and first-order scattered disks. In most cases, this is done by direct summation [62], though a deconvolutive solution exists as well [33, 77].

2.3. Iterative methods

Iterative ptychography constitutes an optimization problem aiming at reconstructing accurate phase images of a specimen. It is conventionally initialized with an object possessing a constant amplitude and phase, respectively equal to 1 and 0, and with a non-aberrated probe.

The original PIE algorithm [63, 64] can generally be considered as originating from the Gerchberg-Saxton algorithm [78, 79], where the phase information is retrieved via the replacement of the calculated amplitude of the exit wave, typically in two distinct optical planes or more, by the experimental amplitude and/or a support constraint. In PIE, this concept is extended to the situation where a single optical plane is used for the acquisition of intensity, typically the far-field, and where illumination conditions are varied, specifically by shifting the probe. An update function is then defined for each probe position, capturing the difference between the original exit wave in real space and the one obtained after replacing the amplitude in reciprocal space. A multiplying factor, sometimes referred to as a regularizer [66] and proportional to the probe intensity, is also inserted to limit the updated area in the specimen plane. Iteratively adding this function to the reconstructed object, while treating scan positions sequentially and weighting it with a user-defined update coefficient, permits the retrieval of an object that satisfies equation 8 [80]. The extended version of PIE [65] aims to find both the object and the probe via the same process. The error function is calculated at each inner iteration, which we define as the computation performed for a single probe position, and convergence is assessed by monitoring the evolution of the error metric over successive iterations. Here, an iteration refers to the computation of update functions across the entire batch of probe positions, starting from an initial randomly selected probe position $j = 1$ and continuing until all positions in the batch $j = J$ have been processed.

$$|\tilde{\psi}(\mathbf{K}_r, \mathbf{R}_0)| = \sqrt{I_{\text{CBED}}(\mathbf{K}_r, \mathbf{R}_0)} \quad (8)$$

Many iterative algorithms exist today [64–66, 69, 81–83], with one essential distinction among them being the method of update execution. In the original PIE and ePIE algorithms, the exit wave update is calculated for each probe position and applied individually, following a random order within the complete set of probe positions. This methodology is referred to as a sequential projection (SP)

algorithm [69]. An alternative algorithmic approach, such as ER, involves computing the complete updates of the exit waves prior to their incorporation into the probe and object functions. This is termed as a batch processing (BP) type of algorithm. A hybrid processing (HP) variant exists, known as the WASP [69], which integrates the update calculation method of ER algorithms with the input methodology of ePIE-like algorithms.

Most SP algorithms, such as ePIE, follow a workflow that involves propagating the exit wave, given in equation 2, to the far field by calculating its Fourier transform. The calculated modulus is in turn replaced with the experimental measurement. The corrected wave is then propagated back to real space by calculating its inverse Fourier transform. The final step involves updating the object and probe functions using the following equations:

$$O_{j+1}(\mathbf{r}) = O_j(\mathbf{r}) + \alpha \frac{P_j^*(\mathbf{r})}{|P_j(\mathbf{r})|_{max}^2} (\psi'_j(\mathbf{r}) - \psi_j(\mathbf{r})) \quad (9)$$

$$P_{j+1}(\mathbf{r}) = P_j(\mathbf{r}) + \beta \frac{O_j^*(\mathbf{r})}{|O_j(\mathbf{r})|_{max}^2} (\psi'_j(\mathbf{r}) - \psi_j(\mathbf{r})) \quad (10)$$

$O_j(\mathbf{r})$ represents the current estimate of the object function at probe position j , while $O_{j+1}(\mathbf{r})$ represents the updated object function, that will be used as the estimate for the next calculation. This process continues until all probe positions within the batch of size (J) are taken into account. $\psi_j(\mathbf{r})$ and $\psi'_j(\mathbf{r})$ represent the estimated and updated exit waves, respectively, in real space.

The update strengths α and β regulate the extent to which the updated probe and object functions deviate from their previous states and typically, multiple iterations are necessary for full convergence of the algorithm. The order in which each position is treated is semi-random, as each one them is visited only once. The required number of updates performed is in practice determined by the minimization of an error function in case of a simulated 4D dataset in which the ground truth is already known. In this context, we calculate the sum squared error (SSE).

$$SSE = \frac{1}{J} \sum_{j=1}^J \left(|\psi'_j(\mathbf{K}_r, \mathbf{R}_0)|^2 - |\psi_j(\mathbf{K}_r, \mathbf{R}_0)|^2 \right)^2 \quad (11)$$

The exploration of more efficient regularizers than those used in ePIE led to the development of the regularized ptychographic iterative engine (rPIE). The object and probe updates for rPIE are given by equation 12 and 13 respectively.

$$O_{j+1}(\mathbf{r}) = O_j(\mathbf{r}) + \frac{P_j^*(\mathbf{r}) (\psi'_j(\mathbf{r}) - \psi_j(\mathbf{r}))}{(\alpha - 1) |P_j(\mathbf{r})|^2 + \alpha |P_j(\mathbf{r})|_{max}^2} \quad (12)$$

$$P_{j+1}(\mathbf{r}) = P_j(\mathbf{r}) + \frac{O_j^*(\mathbf{r}) (\psi'_j(\mathbf{r}) - \psi_j(\mathbf{r}))}{(\beta - 1) |O_j(\mathbf{r})|^2 + \beta |O_j(\mathbf{r})|_{max}^2} \quad (13)$$

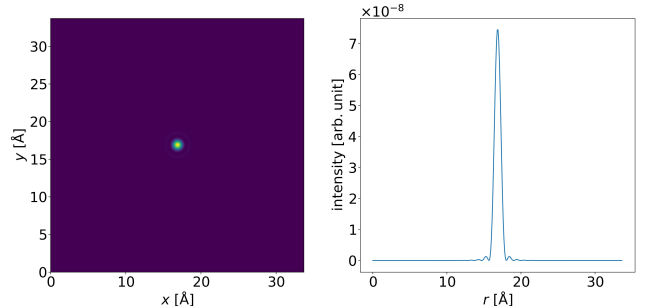


Figure 2: Simulated 2D intensity distribution of an aberration-free focused electron probe (left), along with its corresponding line profile (right). The probe was modeled using a convergence semi-angle of 13 mrad and an acceleration voltage of 200 kV.

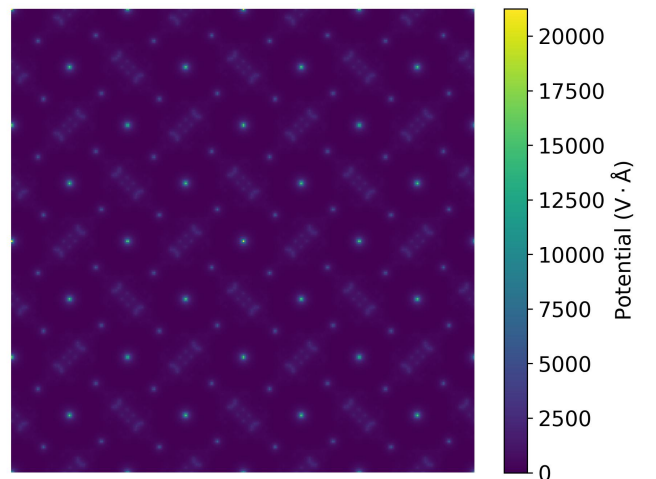


Figure 3: Vertical projection of the electrostatic potential of 2nm thick FAPbBr₃ used for the simulations. The colorbar reflects the values of the projected potential in V.Å

A common criticism of SP, i.e. ePIE-like, algorithms is that they are time-consuming and become increasingly computationally expensive as the batch size or number of iterations increases. This is due to the sequential nature of the updates, where each step depends on the outcome of the previous one, preventing parallelization. Batch processing algorithms such as ER [67, 68] treat the whole data as part of each update. As such, they consist in calculating the exit waves for each probe position and then feeding them into the updated probe and object functions as described in equation 14 and 15. The ability to treat the entire batch of probe positions at once allows parallelizing the calculation of the exit waves and, as a consequence, lowering computation times compared to SP algorithms.

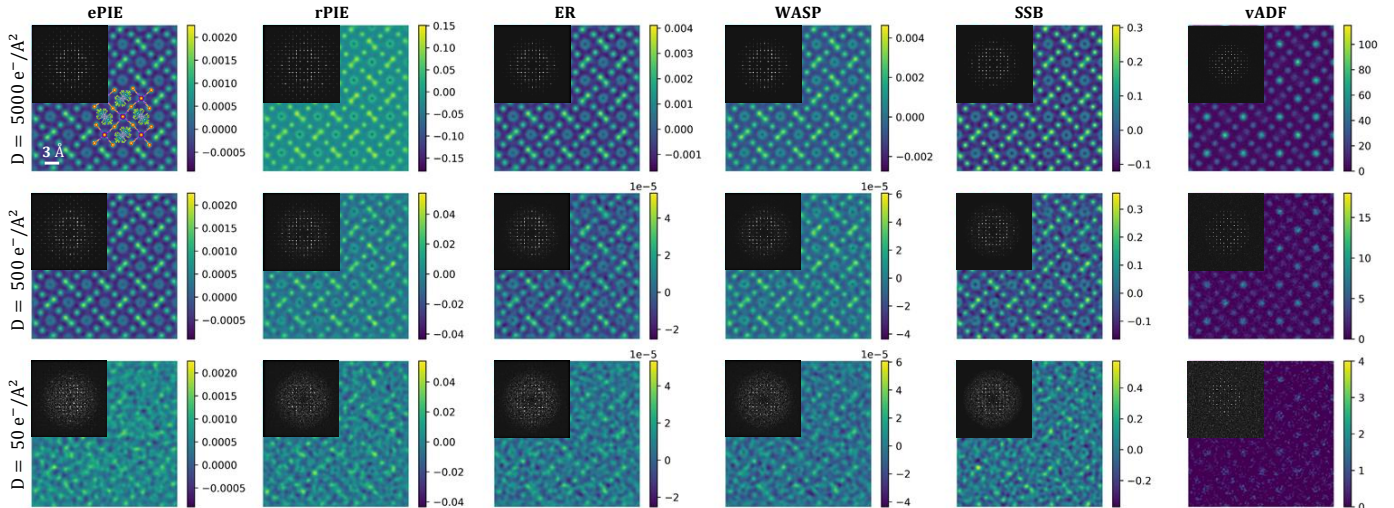


Figure 4: Ptychographic reconstructions and their corresponding Fourier transforms from a simulated 4D dataset of approximately 2 nm thick FAPbBr₃, alongside vADF images, are shown at varying electron doses. The colorbars represent phase values in radians for the ptychographic reconstructions and electron scattering intensities for the vADF images.

$$P_{j+1}(\mathbf{r}) = \frac{\sum_j O_j^*(\mathbf{r})\psi'_j(\mathbf{r})}{\sum_j |O_j(\mathbf{r})|^2}, \quad (14)$$

$$O_{j+1}(\mathbf{r}) = \frac{\sum_j P_j^*(\mathbf{r})\psi'_j(\mathbf{r})}{\sum_j |P_j(\mathbf{r})|^2}, \quad (15)$$

Finally, the WASP algorithm [69] is a hybrid approach that combines the standard update function of rPIE with the batch processing strategy of ER. Integrating rPIE into the algorithm is believed to enhance the convergence speed of ER.

3. Evaluation using simulated data

3.1. Performance of iterative methods and SSB at high and low electron doses

To evaluate the performance of the ptychographic algorithms described above, we simulated a 4D dataset using the abTEM software [84]. The test sample consisted of a 2 nm thick crystal of formamidinium lead bromide (FAPbBr₃), a hybrid organic-inorganic perovskite, where FA (formamidinium) is the organic cation with the chemical formula CH₅N₂⁺. Such hybrid organic-inorganic perovskites are considered promising semiconductors for several optoelectronic technologies, thanks to their tunable bandgap and high carrier mobility among other properties [85, 86].

The simulation used an acceleration voltage of 200 kV, a convergence angle of 13 mrad, and a focused aberration free probe. Sufficient information redundancy is a key factor for a successful iterative ptychography reconstruction, and is achieved via the overlap of the areas illuminated

at adjacent probe positions. Typically, an overlap of approximately 60-80% is sufficient [87]. In this case, a step size of approximately 20 pm was employed to ensure an overlap of about 80%. The propagation of the electron wave through the specimen was performed under the multislice approximation. [88–90]. Owing to the dominant use of low-angle scattering, and hence the minor role of thermal diffuse scattering in this application of electron ptychography, lattice vibrations were not considered. Figure 3 is the resulting projected potential of the 2 nm thick FAPbBr₃ specimen. The probe intensity is given in figure 2. Dose-limited, and hence noisy, data is obtained from the simulated 4D dataset by applying Poisson statistics.

Figure 4 presents the simulated ptychographic reconstructions obtained using the ePIE, rPIE, ER, WASP, and SSB algorithms, along with a virtual annular dark field (vADF) image generated by integrating the intensity over a rather small angular range of 14 to 32 mrad. Note that the pixelated detector employed has a maximum scattering angle of 32 mrad. The ePIE, rPIE, ER, and WASP implementations, originally from Ref. [91], were translated into Python. For SSB, pyPtychoSTEM was used [92].

A total of 30 iterations was employed for the iterative algorithms to ensure sufficient convergence of the reconstruction while balancing computational efficiency. This number was chosen based on prior experience and convergence behavior observed in similar datasets, where further iterations showed diminishing improvements.

The atomic sites of FAPbBr₃ are evident at the highest dose 5000 e⁻/Å² in both the ptychographic reconstructions and the vADF; however, the positions of the organic components in the structure are more discernible in the ptychographic reconstructions, whereas only the heavier Pb and Br columns are visible in the ADF. At 500

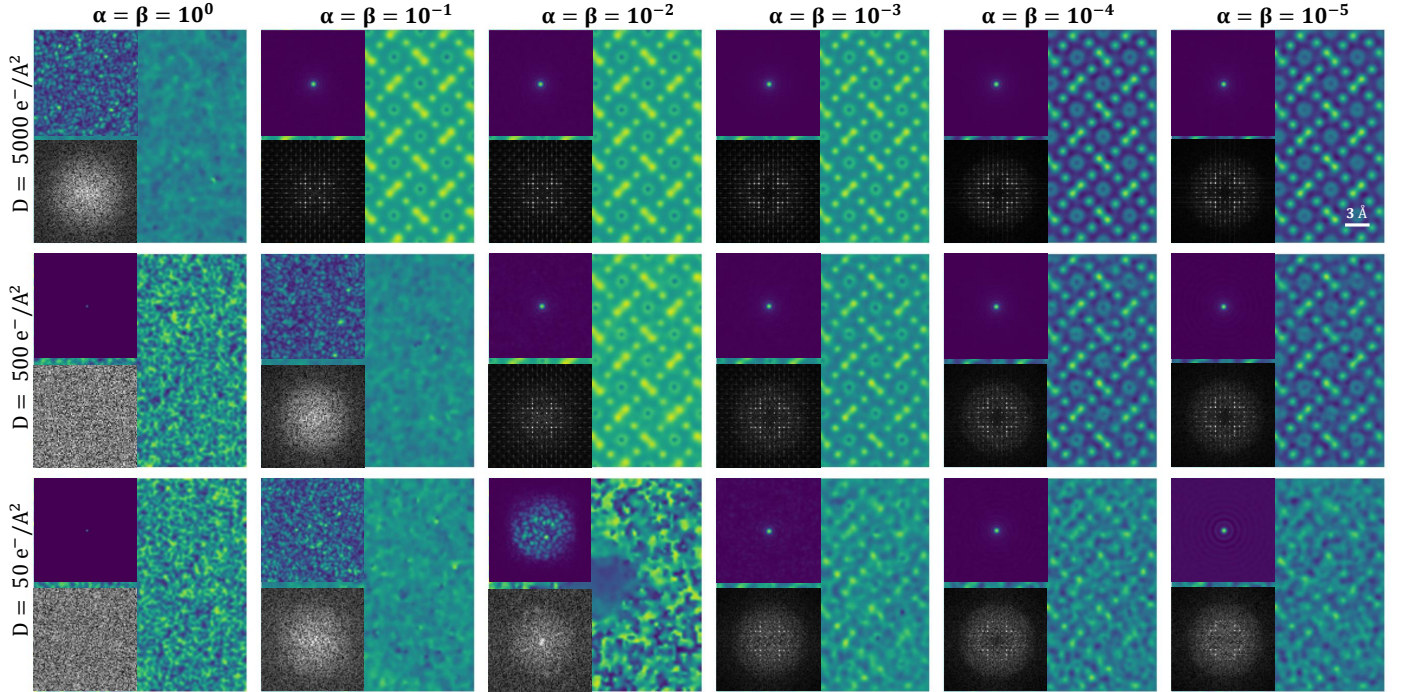


Figure 5: ePIE reconstructions at varying electron doses and update strengths α and β . For each condition, the reconstructed object's phase, the amplitude of its Fourier transform, and the amplitude of the reconstructed probe are shown side by side for direct comparison

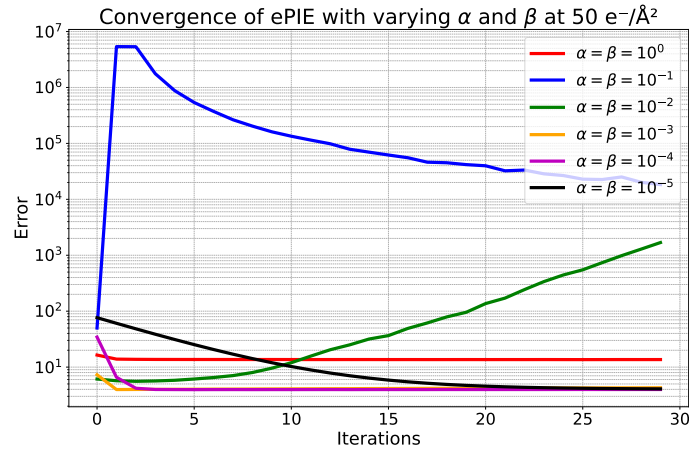


Figure 6: Error curves of ePIE at $50 e^-/\text{\AA}^2$ for varying update strengths.

$e^-/\text{\AA}^2$, both the vADF and theptychographic reconstructions exhibit increased noise, although the contrast from theptychographic reconstructions is better compared to the vADF. At the lowest electron dose used here, the noise level becomes more significant in both imaging modes; the lower frequencies still appear more readily observable in theptychographic reconstructions than in the vADF image.

Notably, this analysis assumes an ideal case in which the sample is not on any support. This differs from experimental conditions, where the sample is often deposited on amorphous carbon or grown on a substrate. Further-

more, contrast reversals observed on the Pb columns in theptychographic reconstructions are primarily caused by the strong projected potentials at these sites. These contrast reversals can be corrected post-reconstruction using the phase offset method [93].

3.2. The effect of the update coefficients on iterative methods

Finding the optimal update coefficients forptychographic reconstructions can be challenging, as excessive modifications of the probe and object functions often lead to a divergence of the reconstruction process, while smaller ones may cause the algorithms to become trapped in local minima. In this section, we investigate the effect of the update strengths at high and low electron doses, for both the extended and the regularized version of PIE, as well as WASP.

Figure 5 depicts ePIE reconstructions based on the simulated 4D dataset presented above, using different update strengths and doses. At the highest dose of $5000 e^-/\text{\AA}^2$ ePIE fails to converge to an image showing the lattice within 30 iterations using $\alpha = \beta = 1$. In addition, the reconstructed probe is clearly incorrect, as evidenced by the probe amplitude displayed alongside the reconstruction in this case. Relatively good object reconstructions are on the other hand achieved for $\alpha = \beta = 10^{-1}$, 10^{-2} , and 10^{-3} , however, the square root of the Fourier transform amplitudes shown as insets reveal artefactual low-frequency components, while the probe's amplitude is being correctly reconstructed at the same values. At the two

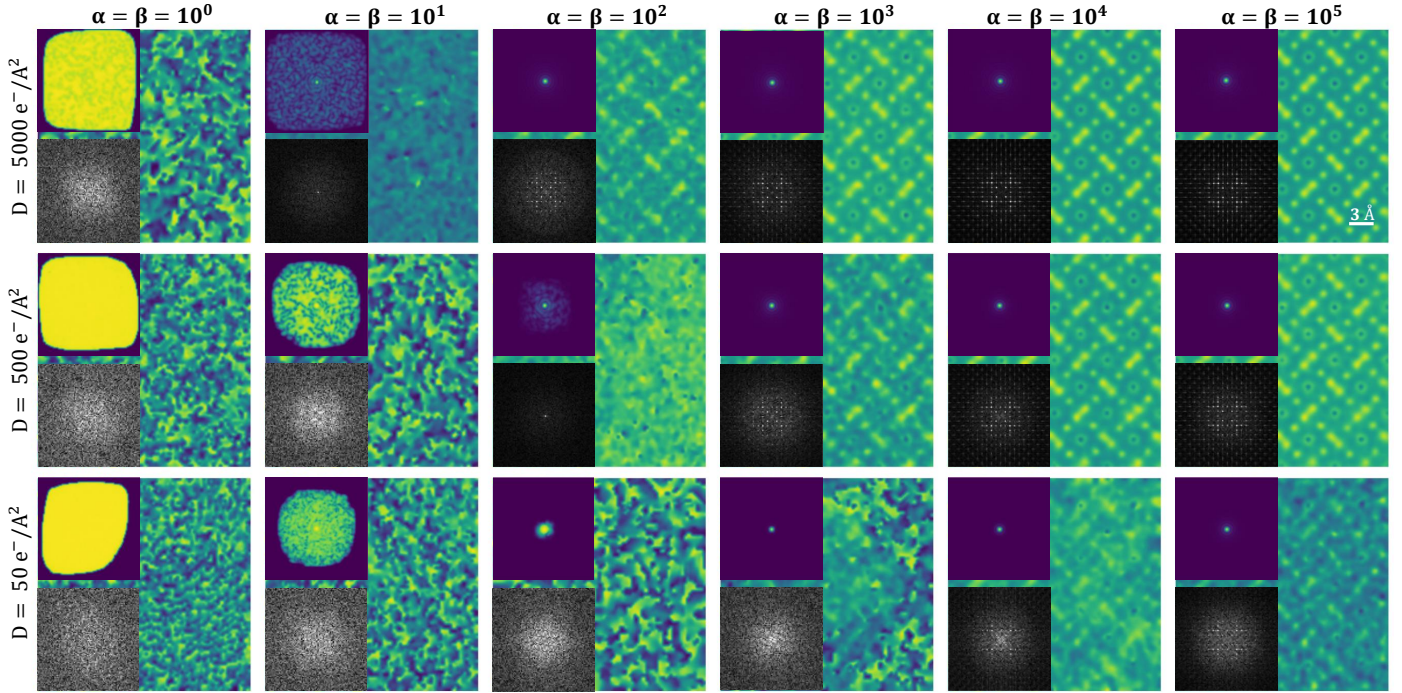


Figure 7: rPIE reconstructions at varying electron doses and update strengths α and β . Each reconstruction is displayed alongside its corresponding FFT and reconstructed probe amplitude for direct comparison.

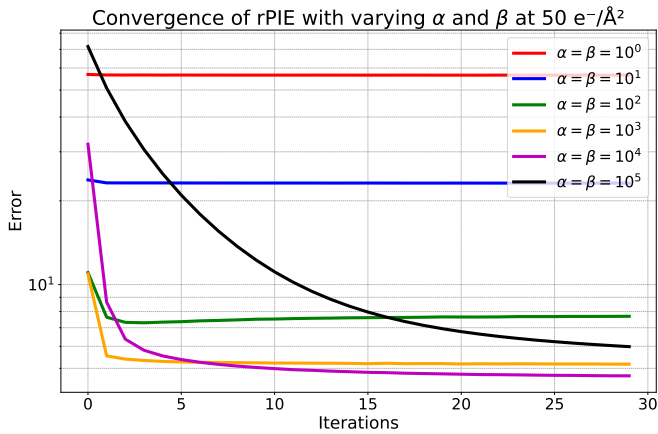


Figure 8: Error curves of rPIE at $50 e^-/\text{\AA}^2$ for varying update strengths.”

lowest update values $\alpha = \beta = 10^{-4}$ and $\alpha = \beta = 10^{-5}$, artifact free reconstructions are obtained as depicted from their respective FFT as well as correctly recovered probes amplitudes. At the intermediate dose of $500 e^-/\text{\AA}^2$ and for the two highest update strength values, the reconstruction fails to capture the specimen’s structure, while the same artefactual low-frequency components are still present at $\alpha = \beta = 10^{-2}$ and 10^{-3} . Similarly to the previous case, the reconstruction of the probe’s amplitude is clearly wrong at the two highest coefficients as depicted by the figure, while both the object and probe’s amplitude are correctly recovered at the two lowest values. At the lowest elec-

tron dose of $50 e^-/\text{\AA}^2$, the algorithm fails to converge at the three highest values of α and β . Finally, for all three doses, improved reconstructions of both the probe and object functions are achieved at values of 10^{-3} , 10^{-4} , and 10^{-5} .

The error curves for the different update strengths, given a dose of $50 e^-/\text{\AA}^2$, are given in figure 6. Note that the object reconstruction begins from a uniform initial guess, with the phase set to zero and the amplitude set to one. As for the probe it is assumed to be focused and aberration-free. The sum squared error (SSE) is calculated according to equation 11 and provided as a function of the number of iterations. First, we observe that, while the error curve shows the error decreasing after the first few iterations at the high values $\alpha = \beta = 1$, the corresponding result does not display useful structural information. This is likely an indication that the algorithm is reaching a local minimum and thus providing an incorrect solution for the object and/or probe functions. At $\alpha = \beta = 10^{-1}$, an increase of the error occurs at the first few iterations, leading to a slow convergence process conserving a high error value for the rest of the calculation, and thus possibly reaching another, different, local minimum. At $\alpha = \beta = 10^{-2}$, the algorithm exhibits a clear diverging behavior. Finally, the error curves for $\alpha = \beta = 10^{-3}$, 10^{-4} and 10^{-5} show the desired convergent behavior, and the resulting images indeed show the lattice. It is worth noting that, for $\alpha = \beta = 10^{-4}$ and 10^{-5} , the initial error starts increasing in the early stage of the reconstruction, but ends up reaching the same minimum error as the threshold value obtained with

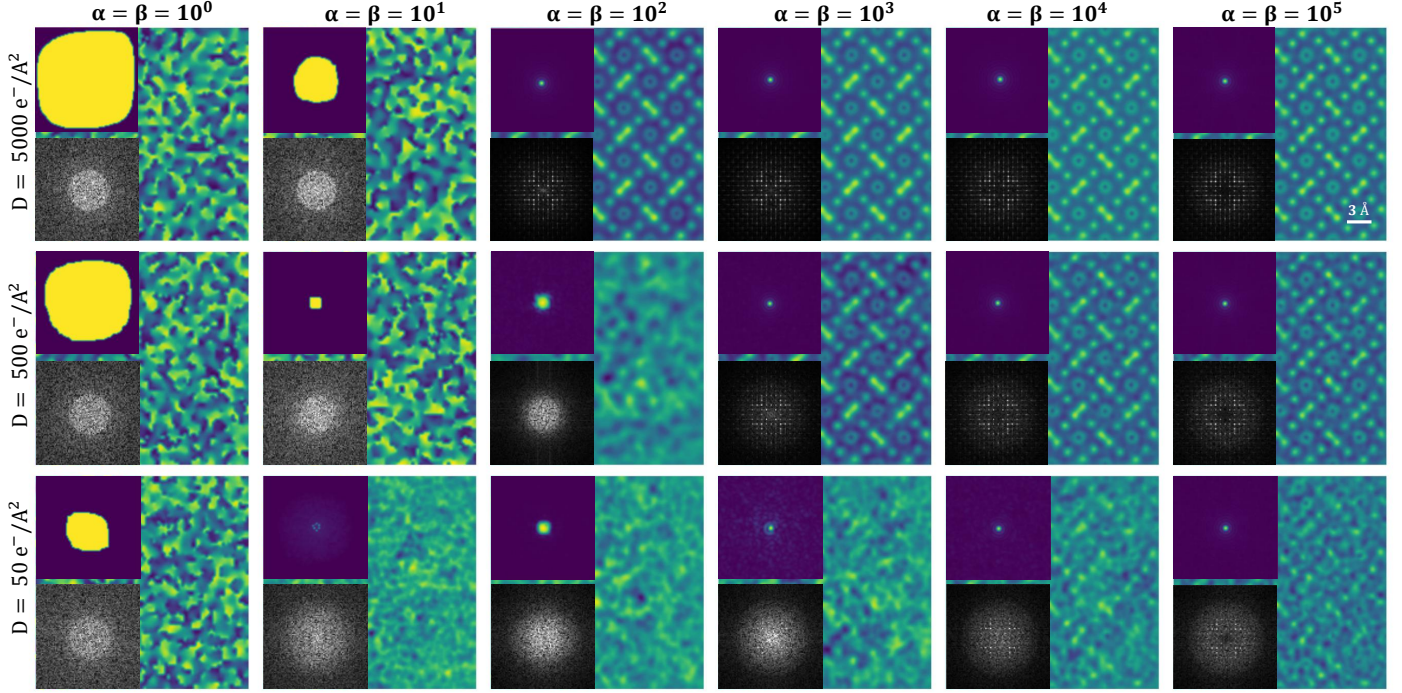


Figure 9: WASP reconstructions at varying electron doses and update strengths α and β . Each reconstruction is displayed alongside its corresponding FFT and reconstructed probe amplitude for direct comparison.

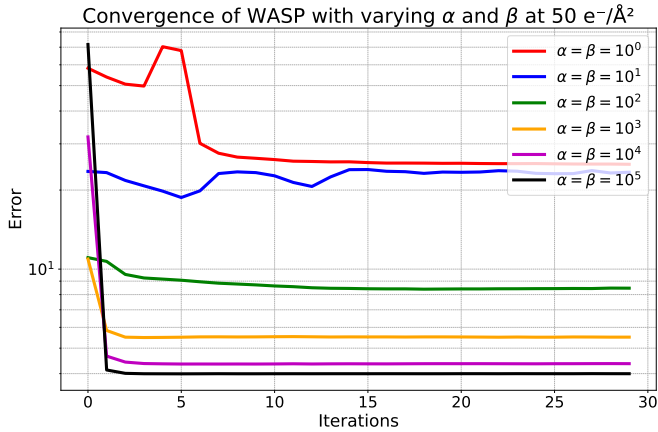


Figure 10: Error curves of WASP at $50 e^-/\text{\AA}^2$ for varying update strengths.

$\alpha = \beta = 10^{-3}$.

The same investigation is next performed with rPIE. Importantly, here, the update coefficients are in the denominator, hence higher values imply a slower modification of the probe and object functions, opposite to the behavior with ePIE. From figure 7 we observe that, at the highest dose of $5000 e^-/\text{\AA}^2$, the reconstruction does not lead to useful structural information for $\alpha = \beta = 1$, whereas successful reconstructions are achievable for higher coefficients. Similar behavior is also observed for the probe's amplitude, which is clearly wrong at the two lowest update coefficients values as shown in the figure.

At $500 e^-/\text{\AA}^2$, the process fails at the three lowest values of α and β while correct convergence is achieved for higher values. At the lowest electron dose of $50 e^-/\text{\AA}^2$, for the four lowest update coefficients neither the lower or higher frequencies of the object are reconstructed, even though the error curves provided in figure 8 show a convergent behavior. This, again, indicates an incorrect solution being reached by the algorithm. Finally, at $\alpha = \beta = 10^4$, a first correct transfer of the specimen's frequencies occurs, as evidenced by the FFT, and the overall contrast of the images further improves for $\alpha = \beta = 10^5$. For the amplitude of the probe, an inaccurate reconstruction is observed at the three lowest coefficients values, whereas a more correct probe distribution is achieved at the highest values. Similarly to the ePIE case, the error curves show the expected convergence, although the initial SSE values increase as the coefficients get larger. The lowest error is achieved for a threshold set of values $\alpha = \beta = 10^4$.

Figure 9 displays results from reconstructions using the WASP algorithm. In general, they show similar features and dose/update strength dependence as ePIE and rPIE. First, at the highest dose, the algorithm fails to converge with the smallest coefficients but converges without artifacts with all others employed. At $500 e^-/\text{\AA}^2$, and at the three lowest coefficient values, neither the lower nor the higher frequencies are reconstructed, while the process still converges at the highest values. Finally, at $50 e^-/\text{\AA}^2$, the calculation starts converging at $\alpha = \beta = 10^3$. Figure 10 depicts the error curves for the different coefficients, at the lowest introduced electron dose, like in the previous

cases. As a first observation, all the curves show convergence for the process, though the lowest converged values is only achievable for the highest two update strengths. Additionally, all the successful reconstructions are free from artifacts. This is interesting, as this indicates that WASP is potentially less susceptible to incorrect solutions and local minima than ePIE and rPIE.

Overall, this simulation study suggests that under low-dose conditions, iterative ptychographic algorithms require small update coefficients for successful reconstructions preferably $\alpha = \beta = 10^{-3}$ for ePIE, and $\alpha = \beta = 10^4$ for rPIE and WASP. Those values are however specific to the investigated material case and should be adapted to the particular experimental configuration and specimen. Nevertheless, the general trends found for the dependencies on dose and update coefficients, for all investigated algorithms, can reasonably be expected to remain for most applications.

4. Evaluation using experimental data

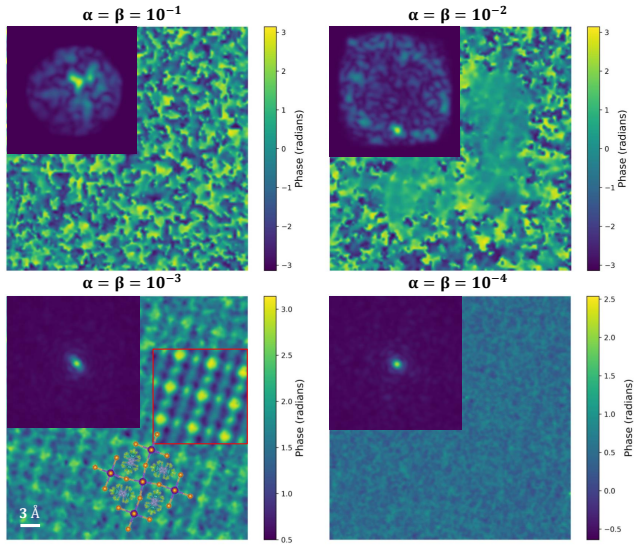


Figure 11: ePIE reconstructions of FaPbBr_3 at varying update strengths using an experimental dataset acquired with a dose of $50 e^-/\text{\AA}$, shown with the corresponding reconstructed probe amplitudes. The 4D-STEM data of the nanocrystal (NC) depicted in the reconstruction for $\alpha = \beta = 10^{-3}$ was averaged using template matching and is presented alongside the reconstruction.

To validate the simulation study presented in section 3, a 4D dataset was experimentally obtained from a FAPbBr_3 nanocrystal, with a thickness approximately equal to 10 nm. The measurements were conducted with an acceleration voltage of 200 kV and a semi-convergence angle of 13 mrad, similar to the parameters chosen in the simulation study. The dataset was acquired using a Timepix3 camera [53, 55], with a dwell time of 1 microsecond. The electron dose was approximately $50 e^-/\text{\AA}^2$. The scan window encompassed 2048×2048 probe positions spread across an area of $10 \times 10 \text{ nm}^2$, and the CBED patterns were binned by a factor of four to 64×64 .

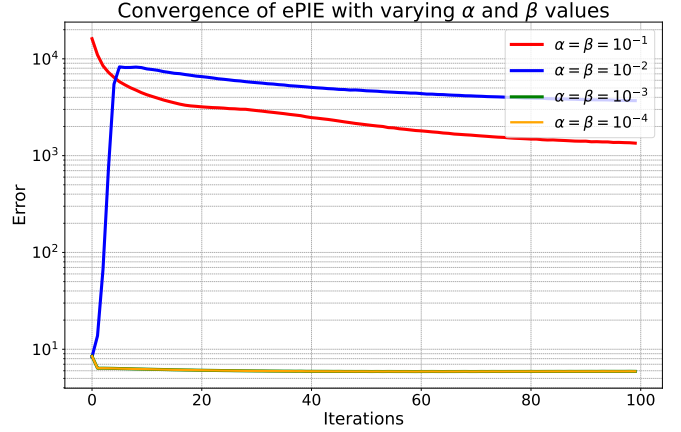


Figure 12: Error curves for ePIE reconstructions at varying update strengths using an experimental dataset acquired with a dose of $50 e^-/\text{\AA}^2$.

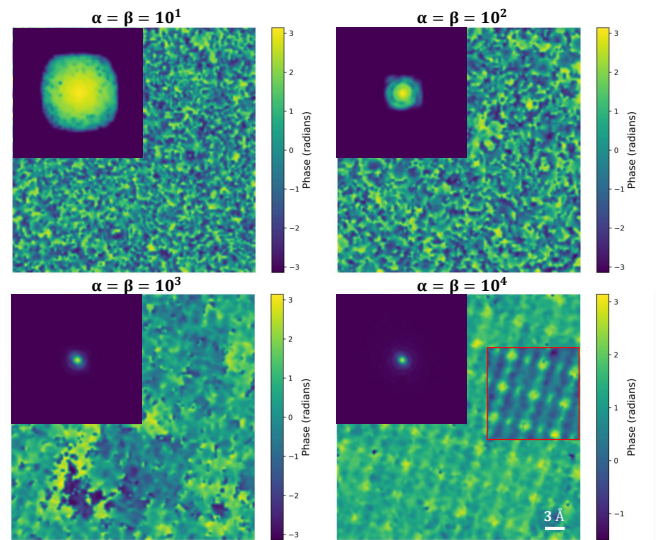


Figure 13: rPIE reconstructions of FaPbBr_3 at varying update strengths using an experimental dataset acquired with a dose of $50 e^-/\text{\AA}$, shown with the corresponding reconstructed probe amplitudes. The 4D-STEM data of the nanocrystal (NC) depicted in the reconstruction for $\alpha = \beta = 10^4$ was averaged using template matching and is presented alongside the reconstruction.

Figure 11 presents ePIE reconstructions performed on a portion of the scanned surface using 100 iterations and varying update strengths. The optimal reconstruction is achieved with $\alpha = \beta = 10^{-3}$, as corroborated by the error curves in Figure 12. Although higher update values of 10^{-1} and 10^{-2} exhibit convergent trends, they maintain significantly larger errors throughout the process. Notably, an initial increase in error occurs within the first few iterations for $\alpha = \beta = 10^{-2}$, and the resulting reconstruction suggests convergence to a local minimum, indicating an incorrect solution. Conversely, at the lower update setting of $\alpha = \beta = 10^{-4}$, the error curve converges to a minimum similar to the 10^{-3} case; however, after 100 iterations, the

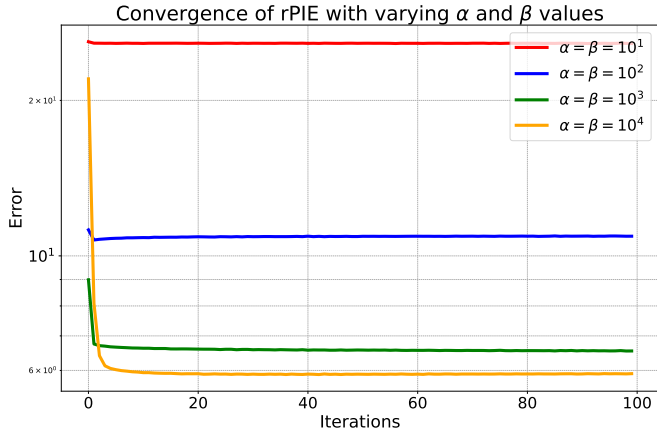


Figure 14: Error curves for rPIE reconstructions at varying update strengths using an experimental dataset acquired with a dose of $50 \text{ e}^-/\text{\AA}^2$.

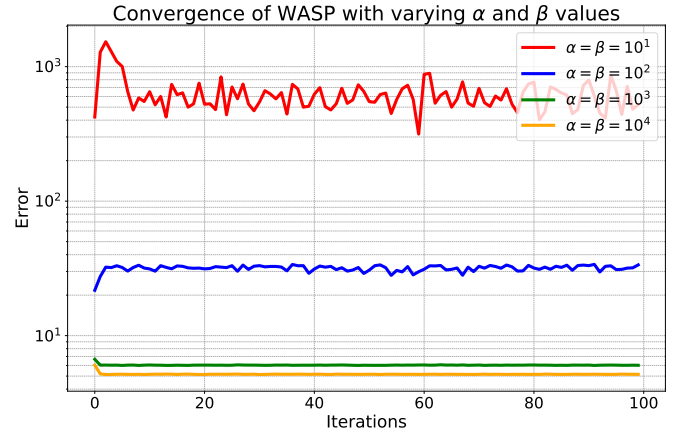


Figure 16: Error curves for WASP reconstructions at varying update strengths using an experimental dataset acquired with a dose of $50 \text{ e}^-/\text{\AA}^2$.

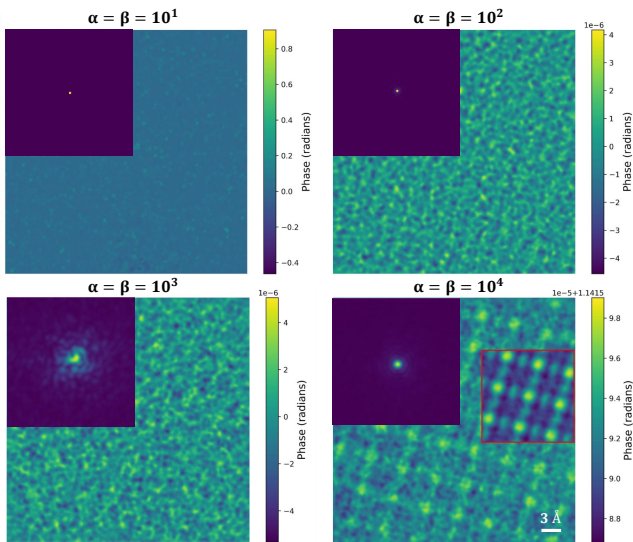


Figure 15: WASP reconstructions of FaPbBr_3 at varying update strengths using an experimental dataset acquired with a dose of $50 \text{ e}^-/\text{\AA}$, shown with the corresponding reconstructed probe amplitudes. The 4D-STEM data of the nanocrystal (NC) depicted in the reconstruction for $\alpha = \beta = 10^4$ was averaged using template matching and is presented alongside the reconstruction.

reconstruction still fails to accurately estimate the object function. This suggests that the algorithm is converging more slowly toward the correct object structure and likely requires additional iterations to fully recover it. Additionally, the initial error for this case is slightly higher than that of the 10^{-3} setting.

Figure 13 illustrates rPIE reconstructions using the same dataset. With update coefficients set to $\alpha = \beta = 10^4$, both the probe and object functions are successfully retrieved, and the algorithm exhibits stable convergence toward a minimal error. As shown in Figure 14, lower update coefficients of $\alpha = \beta = 10^1, 10^2$, and 10^3 still produce convergence, but the algorithm settles at notably higher error

values after 100 iterations. This suggests entrapment in erroneous local minima, clearly visible in the reconstructions of Figure 13.

Figure 15 displays WASP reconstructions performed on the same dataset with various update coefficients. The most accurate probe and object reconstructions correspond to $\alpha = \beta = 10^4$, consistent with the minimum error shown in Figure 16. Lower update values of $\alpha = \beta = 10^1, 10^2$, and 10^3 yield higher minimum errors and less precise reconstructions, as also demonstrated in Figure 15.

5. Conclusion

Since the introduction of the original PIE algorithm [64], several other iterative methods have emerged, including ePIE [65], rPIE [66], WASP [69], and ER [68], among others. The ePIE and rPIE solutions, which are sequential projection algorithms, are similar in their approach to updating the probe and object functions and differ in the used regularizer. WASP, conversely, relies on hybrid processing: it adopts the structural framework of the conventional ER method while incorporating an ePIE-like update function as input.

SP and HP algorithm types require appropriate update coefficients to ensure convergence, particularly at low electron doses. Through the analysis of both simulated and experimental 4D datasets of a thin FAPbBr_3 specimen, we conclude that ePIE, rPIE, and WASP necessitate relatively small steps to facilitate convergence. Furthermore, we note that the initial reconstruction error increases when the update coefficients are reduced below a certain threshold. These observations underscore the importance of carefully selecting appropriate parameters to achieve convergence and accurate reconstructions, particularly under low electron dose conditions. They also emphasize the existence of critical threshold values, beyond which the algorithm's performance becomes susceptible to entrapment in local minima.

By systematically comparing the behavior of these iterative algorithms across multiple parameter regimes, our work reinforces the importance of algorithm-specific coefficient calibration and contributes to a more nuanced understanding of the optimization landscape in iterative ptychographic phase retrieval methods. The observation that performance degrades outside certain coefficient thresholds raises deeper questions about algorithm robustness, reproducibility, convergence dynamics, and susceptibility to local minimum areas that are not yet fully understood. Our contribution offers practical guidelines for effectively deploying these algorithms in experimental 4D-STEM applications, while also setting the stage for future studies aiming at improving reconstruction strategies. In summary, the insights presented here lay the groundwork for developing semi or fully automated iterative phase retrieval algorithms that are more robust and adaptable to changing conditions, such as varying dose levels.

CRedit authorship contribution

T.C.: Conceptualization, Software, Investigation, Formal analysis, Writing – original draft. **S.L.:** Software, Formal analysis, Investigation, review editing. **H.L.L.R.:** Conceptualization, Supervision, Writing – review editing. **C.H.:** Software, Formal analysis, Investigation, review. **N.J.S.:** Data acquisition, review. **S.B.:** Supervision, Writing – review editing. **T.J.P.:** Supervision, Conceptualization, Funding acquisition, Writing – review editing. **J.V.:** Funding acquisition, Supervision, Writing – review editing.

Declaration of competing interest

The authors declare that they have no known competing financial interests or personal relationships that could have appeared to influence the work reported in this paper.

Data availability

Data will be made available on request.

Acknowledgments

The authors kindly thank Prof. Andrew Maiden (EEE Department, University of Sheffield, Sheffield, United Kingdom) for assisting with the preliminary implementations of the original software and for his valuable insights.

J.V. and **T.C.** acknowledge funding from the Flemish Government iBOF project PERsist. **S.B.** and **L.M.** acknowledge funding from the Research Foundation - Flanders (FWO) through project funding (Grant No. G0A7723N). **N.J.S.** acknowledges financial support from the Research

Foundation - Flanders (FWO) through a postdoctoral fellowship (Grant No. 12AAO25N). **H.L.L.R.** and **J.V.** acknowledge further funding from the Horizon 2020 research and innovation programme (European Union), under grant agreement No 101017720 (FET-Proactive EBEAM). **J.V.** and **T.P.** acknowledge funding from the Flemish Government FWO project under grant No. G013122N.

References

- [1] R. F. Egerton, Dose measurement in the TEM and STEM, *Ultramicroscopy* 229 (2021) 113363. doi:10.1016/j.ultramic.2021.113363. URL <https://www.sciencedirect.com/science/article/pii/S0304399121001455>
- [2] R. Erni, M. D. Rossell, C. Kisielowski, U. Dahmen, Atomic-Resolution Imaging with a Sub-50-pm Electron Probe, *Physical Review Letters* 102 (9) (2009) 096101, publisher: American Physical Society. doi:10.1103/PhysRevLett.102.096101. URL <https://link.aps.org/doi/10.1103/PhysRevLett.102.096101>
- [3] P. E. Batson, N. Dellby, O. L. Krivanek, Sub-ångstrom resolution using aberration corrected electron optics, *Nature* 418 (6898) (2002) 617–620, publisher: Nature Publishing Group. doi:10.1038/nature00972. URL <https://www.nature.com/articles/nature00972>
- [4] Q. Chen, C. Dwyer, G. Sheng, C. Zhu, X. Li, C. Zheng, Y. Zhu, Imaging Beam-Sensitive Materials by Electron Microscopy, *Advanced Materials* 32 (16) (2020) 1907619. doi:10.1002/adma.201907619. URL <https://onlinelibrary.wiley.com/doi/10.1002/adma.201907619>
- [5] R. Egerton, Mechanisms of radiation damage in beam-sensitive specimens, for TEM accelerating voltages between 10 and 300 kV, *Microscopy Research and Technique* 75 (11) (2012) 1550–1556. doi:10.1002/jemt.22099. URL <https://analyticalsciencejournals.onlinelibrary.wiley.com/doi/10.1002/jemt.22099>
- [6] R. Egerton, Control of radiation damage in the TEM, *Ultramicroscopy* 127 (2013) 100–108. doi:10.1016/j.ultramic.2012.07.006. URL <https://linkinghub.elsevier.com/retrieve/pii/S0304399112001763>
- [7] R. Egerton, Radiation damage to organic and inorganic specimens in the TEM, *Micron* 119 (2019) 72–87. doi:10.1016/j.micron.2019.01.005. URL <https://linkinghub.elsevier.com/retrieve/pii/S0968432818304359>
- [8] T. Susi, J. C. Meyer, J. Kotakoski, Quantifying transmission electron microscopy irradiation effects using two-dimensional materials, *Nature Reviews Physics* 1 (6) (2019) 397–405. doi:10.1038/s42254-019-0058-y. URL <https://www.nature.com/articles/s42254-019-0058-y>
- [9] J. C. Meyer, F. Eder, S. Kurasch, V. Skakalova, J. Kotakoski, H. J. Park, S. Roth, A. Chuvilin, S. Eyhusen, G. Benner, A. V. Krasheninnikov, U. Kaiser, Accurate Measurement of Electron Beam Induced Displacement Cross Sections for Single-Layer Graphene, *Physical Review Letters* 108 (19) (2012) 196102. doi:10.1103/PhysRevLett.108.196102. URL <https://link.aps.org/doi/10.1103/PhysRevLett.108.196102>
- [10] A. Scheid, Y. Wang, M. Jung, T. Heil, D. Moia, J. Maier, P. A. Van Aken, Electron Ptychographic Phase Imaging of Beam-sensitive All-inorganic Halide Perovskites Using Four-dimensional Scanning Transmission Electron Microscopy, *Microscopy and Microanalysis* 29 (3) (2023) 869–878. doi:10.1093/micmic/ozad017. URL <https://academic.oup.com/mam/article/29/3/869/7131445>

- [11] J. Satta, A. Casu, D. Chiriu, C. M. Carbonaro, L. Stagi, P. C. Ricci, Formation Mechanisms and Phase Stability of Solid-State Grown CsPbI₃ Perovskites, *Nanomaterials* 11 (7) (2021) 1823, number: 7 Publisher: Multidisciplinary Digital Publishing Institute. doi:10.3390/nano11071823.
URL <https://www.mdpi.com/2079-4991/11/7/1823>
- [12] K. Dhivyaprasath, M. Ashok, Degradation Behavior of Methylammonium Lead Iodide (CH₃NH₃PbI₃) Perovskite Film in Ambient Atmosphere and Device, *Solar Energy* 255 (2023) 89–98. doi:10.1016/j.solener.2023.03.021.
URL <https://linkinghub.elsevier.com/retrieve/pii/S0038092X23001767>
- [13] N. J. Schrenker, T. Braeckvelt, A. De Backer, N. Livakas, C.-P. Yu, T. Friedrich, M. B. J. Roeflaers, J. Hofkens, J. Verbeeck, L. Manna, V. Van Speybroeck, S. Van Aert, S. Bals, Investigation of the Octahedral Network Structure in Formamidineum Lead Bromide Nanocrystals by Low-Dose Scanning Transmission Electron Microscopy, *Nano Letters* 24 (35) (2024) 10936–10942. doi:10.1021/acs.nanolett.4c02811.
URL <https://pubs.acs.org/doi/10.1021/acs.nanolett.4c02811>
- [14] O. Ugurlu, J. Haus, A. A. Gunawan, M. G. Thomas, S. Maheshwari, M. Tsapatsis, K. A. Mkhoyan, Radiolysis to knock-on damage transition in zeolites under electron beam irradiation, *Physical Review B* 83 (11) (2011) 113408. doi:10.1103/PhysRevB.83.113408.
URL <https://link.aps.org/doi/10.1103/PhysRevB.83.113408>
- [15] L. Liu, N. Wang, C. Zhu, X. Liu, Y. Zhu, P. Guo, L. Alfilfil, X. Dong, D. Zhang, Y. Han, Direct Imaging of Atomically Dispersed Molybdenum that Enables Location of Aluminum in the Framework of Zeolite ZSM-5, *Angewandte Chemie International Edition* 59 (2) (2020) 819–825, eprint: <https://onlinelibrary.wiley.com/doi/pdf/10.1002/anie.201909834>. doi:10.1002/anie.201909834.
URL <https://onlinelibrary.wiley.com/doi/abs/10.1002/anie.201909834>
- [16] K. Ooe, T. Seki, K. Yoshida, Y. Kohno, Y. Ikuhara, N. Shibata, Direct imaging of local atomic structures in zeolite using optimum bright-field scanning transmission electron microscopy, *Science Advances* 9 (31) (2023) eadf6865, publisher: American Association for the Advancement of Science. doi:10.1126/sciadv.adf6865.
URL <https://www.science.org/doi/full/10.1126/sciadv.adf6865>
- [17] H. Furukawa, K. E. Cordova, M. O’Keeffe, O. M. Yaghi, The Chemistry and Applications of Metal-Organic Frameworks, *Science* 341 (6149) (2013) 1230444, publisher: American Association for the Advancement of Science. doi:10.1126/science.1230444.
URL <https://www.science.org/doi/10.1126/science.1230444>
- [18] D. Yang, B. C. Gates, Catalysis by Metal Organic Frameworks: Perspective and Suggestions for Future Research, *ACS Catalysis* 9 (3) (2019) 1779–1798, publisher: American Chemical Society. doi:10.1021/acscatal.8b04515.
URL <https://doi.org/10.1021/acscatal.8b04515>
- [19] A. Bavykina, N. Kolobov, I. S. Khan, J. A. Bau, A. Ramirez, J. Gascon, Metal–Organic Frameworks in Heterogeneous Catalysis: Recent Progress, New Trends, and Future Perspectives, *Chemical Reviews* 120 (16) (2020) 8468–8535, publisher: American Chemical Society. doi:10.1021/acs.chemrev.9b00685.
URL <https://doi.org/10.1021/acs.chemrev.9b00685>
- [20] S. Kavak, D. Jannis, A. De Backer, D. A. Esteban, A. Annys, S. Carrasco, J. Ferrando-Ferrero, R. M. Guerrero, P. Horcajada, J. Verbeeck, S. Van Aert, S. Bals, High-resolution electron microscopy imaging of MOFs at optimized electron dose, *Journal of Materials Chemistry A* (2025) 10.1039/D4TA06724Jdoi: 10.1039/D4TA06724J.
URL <https://xlink.rsc.org/?DOI=D4TA06724J>
- [21] R. M. Glaeser, Limitations to significant information in biological electron microscopy as a result of radiation damage, *Journal of Ultrastructure Research* 36 (3) (1971) 466–482. doi: 10.1016/S0022-5320(71)80118-1.
URL <https://www.sciencedirect.com/science/article/pii/S0022532071801181>
- [22] R. Henderson, P. N. T. Unwin, Three-dimensional model of purple membrane obtained by electron microscopy, *Nature* 257 (5521) (1975) 28–32, publisher: Nature Publishing Group. doi:10.1038/257028a0.
URL <https://www.nature.com/articles/257028a0>
- [23] B. Küçüköğlü, I. Mohammed, R. C. Guerrero-Ferreira, S. M. Ribet, G. Varnavides, M. L. Leidl, K. Lau, S. Nazarov, A. Myasnikov, M. Kube, J. Radecke, C. Sachse, K. Müller-Caspary, C. Ophus, H. Stahlberg, Low-dose cryo-electron ptychography of proteins at sub-nanometer resolution, *Nature Communications* 15 (1) (2024) 8062, publisher: Nature Publishing Group. doi:10.1038/s41467-024-52403-5.
URL <https://www.nature.com/articles/s41467-024-52403-5>
- [24] L. Zhou, J. Song, J. S. Kim, X. Pei, C. Huang, M. Boyce, L. Mendonça, D. Clare, A. Siebert, C. S. Allen, E. Liberti, D. Stuart, X. Pan, P. D. Nellist, P. Zhang, A. I. Kirkland, P. Wang, Low-dose phase retrieval of biological specimens using cryo-electron ptychography, *Nature Communications* 11 (1) (2020) 2773, publisher: Nature Publishing Group. doi:10.1038/s41467-020-16391-6.
URL <https://www.nature.com/articles/s41467-020-16391-6>
- [25] I. Lazić, E. G. T. Bosch, S. Lazar, Phase contrast STEM for thin samples: Integrated differential phase contrast, *Ultramicroscopy* 160 (2016) 265–280. doi:10.1016/j.ultramic.2015.10.011.
URL <https://www.sciencedirect.com/science/article/pii/S0304399115300449>
- [26] I. Lazić, M. Wirix, M. L. Leidl, F. De Haas, D. Mann, M. Beckers, E. V. Pechnikova, K. Müller-Caspary, R. Egoavil, E. G. T. Bosch, C. Sachse, Single-particle cryo-EM structures from iDPC-STEM at near-atomic resolution, *Nature Methods* 19 (9) (2022) 1126–1136. doi:10.1038/s41592-022-01586-0.
URL <https://www.nature.com/articles/s41592-022-01586-0>
- [27] X. Li, J. Wang, X. Liu, L. Liu, D. Cha, X. Zheng, A. A. Yousef, K. Song, Y. Zhu, D. Zhang, Y. Han, Direct Imaging of Tunable Crystal Surface Structures of MOF MIL-101 Using High-Resolution Electron Microscopy, *Journal of the American Chemical Society* 141 (30) (2019) 12021–12028, publisher: American Chemical Society. doi:10.1021/jacs.9b04896.
URL <https://doi.org/10.1021/jacs.9b04896>
- [28] H. Yang, T. J. Pennycook, P. D. Nellist, Efficient phase contrast imaging in STEM using a pixelated detector. Part II: Optimisation of imaging conditions, *Ultramicroscopy* 151 (2015) 232–239. doi:10.1016/j.ultramic.2014.10.013.
URL <https://linkinghub.elsevier.com/retrieve/pii/S0304399114002058>
- [29] C. M. O’Leary, C. S. Allen, C. Huang, J. S. Kim, E. Liberti, P. D. Nellist, A. I. Kirkland, Phase reconstruction using fast binary 4D STEM data, *Applied Physics Letters* 116 (12) (2020) 124101. doi:10.1063/1.5143213.
URL <https://doi.org/10.1063/1.5143213>
- [30] C. M. O’Leary, G. T. Martinez, E. Liberti, M. J. Humphry, A. I. Kirkland, P. D. Nellist, Contrast transfer and noise considerations in focused-probe electron ptychography, *Ultramicroscopy* 221 (2021) 113189. doi:10.1016/j.ultramic.2020.113189.
URL <https://www.sciencedirect.com/science/article/pii/S0304399120303314>
- [31] B. Hao, Z. Ding, X. Tao, P. D. Nellist, H. E. Assender, Atomic-scale imaging of polyvinyl alcohol crystallinity using electron ptychography, *Polymer* 284 (2023) 126305. doi:10.1016/j.polymer.2023.126305.
URL <https://www.sciencedirect.com/science/article/pii/S0032386123006353>

- [32] Z. Dong, E. Zhang, Y. Jiang, Q. Zhang, A. Mayoral, H. Jiang, Y. Ma, Atomic-Level Imaging of Zeolite Local Structures Using Electron Ptychography, *Journal of the American Chemical Society* 145 (12) (2023) 6628–6632, publisher: American Chemical Society. doi:10.1021/jacs.2c12673.
URL <https://doi.org/10.1021/jacs.2c12673>
- [33] H. L. L. Robert, M. L. Leidl, K. Müller-Caspary, J. Verbeeck, Benchmarking analytical electron ptychography methods for the low-dose imaging of beam-sensitive materials, arXiv:2501.08874 [physics] (Jan. 2025). doi:10.48550/arXiv.2501.08874.
URL <http://arxiv.org/abs/2501.08874>
- [34] G. Li, M. Xu, W.-Q. Tang, Y. Liu, C. Chen, D. Zhang, L. Liu, S. Ning, H. Zhang, Z.-Y. Gu, Z. Lai, D. A. Muller, Y. Han, Atomically resolved imaging of radiation-sensitive metal-organic frameworks via electron ptychography, *Nature Communications* 16 (1) (2025) 914, publisher: Nature Publishing Group. doi:10.1038/s41467-025-56215-z.
URL <https://www.nature.com/articles/s41467-025-56215-z>
- [35] J. G. Lozano, G. T. Martinez, L. Jin, P. D. Nellist, P. G. Bruce, Low-Dose Aberration-Free Imaging of Li-Rich Cathode Materials at Various States of Charge Using Electron Ptychography, *Nano Letters* 18 (11) (2018) 6850–6855, publisher: American Chemical Society. doi:10.1021/acs.nanolett.8b02718.
URL <https://doi.org/10.1021/acs.nanolett.8b02718>
- [36] J. R. Fienup, Reconstruction of an object from the modulus of its Fourier transform, *Optics Letters* 3 (1) (1978) 27. doi:10.1364/OL.3.000027.
URL <https://opg.optica.org/abstract.cfm?URI=ol-3-1-27>
- [37] J. R. Fienup, Phase retrieval algorithms: a comparison, *Applied Optics* 21 (15) (1982) 2758. doi:10.1364/AO.21.002758.
URL <https://opg.optica.org/abstract.cfm?URI=ao-21-15-2758>
- [38] J. R. Fienup, Reconstruction of a complex-valued object from the modulus of its Fourier transform using a support constraint, *Journal of the Optical Society of America A* 4 (1) (1987) 118. doi:10.1364/JOSA.4.000118.
URL <https://opg.optica.org/abstract.cfm?URI=josaa-4-1-118>
- [39] J. Miao, D. Sayre, H. N. Chapman, Phase retrieval from the magnitude of the Fourier transforms of nonperiodic objects, *Journal of the Optical Society of America A* 15 (6) (1998) 1662. doi:10.1364/JOSA.15.001662.
URL <https://opg.optica.org/abstract.cfm?URI=josaa-15-6-1662>
- [40] J. Miao, P. Charalambous, J. Kirz, D. Sayre, Extending the methodology of X-ray crystallography to allow imaging of micrometre-sized non-crystalline specimens, *Nature* 400 (6742) (1999) 342–344. doi:10.1038/22498.
URL <https://www.nature.com/articles/22498>
- [41] W. Hoppe, Beugung im inhomogenen Primärstrahlwellenfeld. III. Amplituden- und Phasenbestimmung bei unperiodischen Objekten, *Acta Crystallographica Section A* 25 (4) (1969) 508–514. doi:10.1107/S0567739469001069.
URL <https://scripts.iucr.org/cgi-bin/paper?S0567739469001069>
- [42] W. Hoppe, G. Strube, Beugung in inhomogenen Primärstrahlwellenfeld. II. Lichtoptische Analogiever suche zur Phasenmessung von Gitterinterferenzen, *Acta Crystallographica Section A* 25 (4) (1969) 502–507. doi:10.1107/S0567739469001057.
URL <https://scripts.iucr.org/cgi-bin/paper?S0567739469001057>
- [43] W. Hoppe, Beugung im inhomogenen Primärstrahlwellenfeld. I. Prinzip einer Phasenmessung von Elektronenbeugungsinterferenzen, *Acta Crystallographica Section A* 25 (4) (1969) 495–501. doi:10.1107/S0567739469001045.
URL <https://scripts.iucr.org/cgi-bin/paper?S0567739469001045>
- [44] G. McMullan, D. M. Cattermole, S. Chen, R. Henderson, X. Llopart, C. Summerfield, L. Tlustos, A. R. Faruqi, Electron imaging with Medipix2 hybrid pixel detector, *Ultramicroscopy* 107 (4) (2007) 401–413. doi:10.1016/j.ultramic.2006.10.005.
URL <https://www.sciencedirect.com/science/article/pii/S0304399106001963>
- [45] X. Llopart, R. Ballabriga, M. Campbell, L. Tlustos, W. Wong, Timepix, a 65k programmable pixel readout chip for arrival time, energy and/or photon counting measurements, *Nuclear Instruments and Methods in Physics Research Section A: Accelerators, Spectrometers, Detectors and Associated Equipment* 581 (1) (2007) 485–494. doi:10.1016/j.nima.2007.08.079.
URL <https://www.sciencedirect.com/science/article/pii/S0168900207017020>
- [46] R. Ballabriga, M. Campbell, E. Heijne, X. Llopart, L. Tlustos, W. Wong, Medipix3: A 64 k pixel detector readout chip working in single photon counting mode with improved spectrometric performance, *Nuclear Instruments and Methods in Physics Research Section A: Accelerators, Spectrometers, Detectors and Associated Equipment* 633 (2011) S15–S18. doi:10.1016/j.nima.2010.06.108.
URL <https://www.sciencedirect.com/science/article/pii/S0168900210012982>
- [47] J. A. Mir, R. Clough, R. MacInnes, C. Gough, R. Plackett, I. Shipsey, H. Sawada, I. MacLaren, R. Ballabriga, D. Maneuski, V. O’Shea, D. McGrouther, A. I. Kirkland, Characterisation of the Medipix3 detector for 60 and 80 keV electrons, *Ultramicroscopy* 182 (2017) 44–53. doi:10.1016/j.ultramic.2017.06.010.
URL <https://www.sciencedirect.com/science/article/pii/S0304399116303989>
- [48] H. Ryll, M. Simson, R. Hartmann, P. Holl, M. Huth, S. Ihle, Y. Kondo, P. Kotula, A. Liebel, K. Müller-Caspary, A. Rosenauer, R. Sagawa, J. Schmidt, H. Soltau, L. Strüder, A pnCCD-based, fast direct single electron imaging camera for TEM and STEM, *Journal of Instrumentation* 11 (04) (2016) P04006. doi:10.1088/1748-0221/11/04/P04006.
URL <https://dx.doi.org/10.1088/1748-0221/11/04/P04006>
- [49] H. T. Philipp, M. W. Tate, K. S. Shanks, L. Mele, M. Peemen, P. Dona, R. Hartong, G. van Veen, Y.-T. Shao, Z. Chen, J. Thom-Levy, D. A. Muller, S. M. Gruner, Very-High Dynamic Range, 10,000 Frames/Second Pixel Array Detector for Electron Microscopy, *Microscopy and Microanalysis* 28 (2) (2022) 425–440. doi:10.1017/S1431927622000174.
URL <https://doi.org/10.1017/S1431927622000174>
- [50] P. Zambon, Enhanced DQE and sub-pixel resolution by single-event processing in counting hybrid pixel electron detectors: A simulation study, *Frontiers in Physics* 11, publisher: Frontiers. doi:10.3389/fphy.2023.1123787.
URL <https://www.frontiersin.org/journals/physics/articles/10.3389/fphy.2023.1123787/full>
- [51] P. Ercius, I. J. Johnson, P. Pelz, B. H. Savitzky, L. Hughes, H. G. Brown, S. E. Zeltmann, S.-L. Hsu, C. C. S. Pedrosa, B. E. Cohen, R. Ramesh, D. Paul, J. M. Joseph, T. Stezelberger, C. Czarnik, M. Lent, E. Fong, J. Ciston, M. C. Scott, C. Ophus, A. M. Minor, P. Denes, The 4D Camera: An 87 kHz Direct Electron Detector for Scanning/Transmission Electron Microscopy, *Microscopy and Microanalysis: The Official Journal of Microscopy Society of America, Microbeam Analysis Society, Microscopical Society of Canada* 30 (5) (2024) 903–912. doi:10.1093/mam/ozae086.
- [52] H. Yang, L. Jones, H. Ryll, M. Simson, H. Soltau, Y. Kondo, R. Sagawa, H. Banba, I. MacLaren, P. D. Nellist, 4D STEM: High efficiency phase contrast imaging using a fast pixelated detector, *Journal of Physics: Conference Series* 644 (2015) 012032. doi:10.1088/1742-6596/644/1/012032.
URL <https://iopscience.iop.org/article/10.1088/1742-6596/644/1/012032>
- [53] T. Poikela, J. Plosila, T. Westerlund, M. Campbell, M. D. Gaspari, X. Llopart, V. Gromov, R. Kluit, M. v. Beuzekom, F. Zappone, V. Zivkovic, C. Brezina, K. Desch, Y. Fu, A. Kruth, Timepix3: a 65K channel hybrid pixel readout chip with simul-

- taneous ToA/ToT and sparse readout, *Journal of Instrumentation* 9 (05) (2014) C05013. doi:10.1088/1748-0221/9/05/C05013.
URL <https://dx.doi.org/10.1088/1748-0221/9/05/C05013>
- [54] X. Llopart, J. Alozy, R. Ballabriga, M. Campbell, R. Casanova, V. Gromov, E. H. M. Heijne, T. Poikela, E. Santin, V. Srisakaran, L. Tlustos, A. Vitkovskiy, Timepix4, a large area pixel detector readout chip which can be tiled on 4 sides providing sub-200 ps timestamp binning, *Journal of Instrumentation* 17 (01) (2022) C01044, publisher: IOP Publishing. doi:10.1088/1748-0221/17/01/C01044.
URL <https://dx.doi.org/10.1088/1748-0221/17/01/C01044>
- [55] D. Jannis, C. Hofer, C. Gao, X. Xie, A. Béché, T. J. Pennycook, J. Verbeeck, Event driven 4D STEM acquisition with a Timepix3 detector: Microsecond dwell time and faster scans for high precision and low dose applications, *Ultramicroscopy* 233 (2022) 113423. doi:10.1016/j.ultramic.2021.113423.
URL <https://www.sciencedirect.com/science/article/pii/S0304399121001996>
- [56] Y. Aaad, J. Baaboura, J.-D. Blazit, M. Tencé, O. Stéphan, M. Kociak, L. H. G. Tizei, Time calibration studies for the Timepix3 hybrid pixel detector in electron microscopy, *Ultramicroscopy* 257 (2024) 113889. doi:10.1016/j.ultramic.2023.113889.
URL <https://www.sciencedirect.com/science/article/pii/S0304399123002061>
- [57] N. Denisov, D. Jannis, A. Orekhov, K. Müller-Caspari, J. Verbeeck, Characterization of a Timepix detector for use in SEM acceleration voltage range, *Ultramicroscopy* 253 (2023) 113777. doi:10.1016/j.ultramic.2023.113777.
URL <https://www.sciencedirect.com/science/article/pii/S0304399123000943>
- [58] J. M. Rodenburg, R. H. T. Bates, The theory of super-resolution electron microscopy via Wigner-distribution deconvolution, *Philosophical Transactions of the Royal Society of London. Series A: Physical and Engineering Sciences* 339 (1655) (1992) 521–553, publisher: Royal Society. doi:10.1098/rsta.1992.0050.
URL <https://royalsocietypublishing.org/doi/10.1098/rsta.1992.0050>
- [59] R. H. T. Bates, J. M. Rodenburg, Sub-ångström transmission microscopy: A fourier transform algorithm for microdiffraction plane intensity information, *Ultramicroscopy* 31 (3) (1989) 303–307. doi:10.1016/0304-3991(89)90052-1.
URL <https://www.sciencedirect.com/science/article/pii/0304399189900521>
- [60] B. C. McCallum, J. M. Rodenburg, Two-dimensional demonstration of Wigner phase-retrieval microscopy in the STEM configuration, *Ultramicroscopy* 45 (3) (1992) 371–380. doi:10.1016/0304-3991(92)90149-E.
URL <https://www.sciencedirect.com/science/article/pii/030439919290149E>
- [61] J. M. Rodenburg, B. C. McCallum, P. D. Nellist, Experimental tests on double-resolution coherent imaging via STEM, *Ultramicroscopy* 48 (3) (1993) 304–314. doi:10.1016/0304-3991(93)90105-7.
URL <https://www.sciencedirect.com/science/article/pii/0304399193901057>
- [62] T. J. Pennycook, A. R. Lupini, H. Yang, M. F. Murfitt, L. Jones, P. D. Nellist, Efficient phase contrast imaging in STEM using a pixelated detector. Part 1: Experimental demonstration at atomic resolution, *Ultramicroscopy* 151 (2015) 160–167. doi:10.1016/j.ultramic.2014.09.013.
URL <https://www.sciencedirect.com/science/article/pii/S0304399114001934>
- [63] H. M. L. Faulkner, J. M. Rodenburg, Movable Aperture Lensless Transmission Microscopy: A Novel Phase Retrieval Algorithm, *Physical Review Letters* 93 (2) (2004) 023903. doi:10.1103/PhysRevLett.93.023903.
URL <https://link.aps.org/doi/10.1103/PhysRevLett.93.023903>
- [64] J. M. Rodenburg, H. M. L. Faulkner, A phase retrieval algorithm for shifting illumination, *Applied Physics Letters* 85 (20) (2004) 4795–4797. doi:10.1063/1.1823034.
URL <https://pubs.aip.org/apl/article/85/20/4795/329473/A-phase-retrieval-algorithm-for-shifting>
- [65] A. M. Maiden, J. M. Rodenburg, An improved ptychographical phase retrieval algorithm for diffractive imaging, *Ultramicroscopy* 109 (10) (2009) 1256–1262. doi:10.1016/j.ultramic.2009.05.012.
URL <https://linkinghub.elsevier.com/retrieve/pii/S0304399109001284>
- [66] A. Maiden, D. Johnson, P. Li, Further improvements to the ptychographical iterative engine, *Optica* 4 (7) (2017) 736–745, publisher: Optica Publishing Group. doi:10.1364/OPTICA.4.000736.
URL <https://opg.optica.org/optica/abstract.cfm?uri=optica-4-7-736>
- [67] P. Thibault, M. Dierolf, O. Bunk, A. Menzel, F. Pfeiffer, Probe retrieval in ptychographic coherent diffractive imaging, *Ultramicroscopy* 109 (4) (2009) 338–343. doi:10.1016/j.ultramic.2008.12.011.
URL <https://www.sciencedirect.com/science/article/pii/S0304399108003458>
- [68] P. Thibault, M. Dierolf, A. Menzel, O. Bunk, C. David, F. Pfeiffer, High-Resolution Scanning X-ray Diffraction Microscopy, *Science* 321 (5887) (2008) 379–382, publisher: American Association for the Advancement of Science. doi:10.1126/science.1158573.
URL <https://www.science.org/doi/10.1126/science.1158573>
- [69] A. Maiden, W. Mei, P. Li, WASP: Weighted Average of Sequential Projections for ptychographic phase retrieval (Jan. 2024). doi:10.1364/opticaopen.24894489.v1.
URL https://preprints.opticaopen.org/articles/preprint/WASP_Weighted_Average_of_Sequential_Projections_for_ptychographic_phase_retrieval/24894489/1
- [70] J. M. Cowley, S. Iijima, Electron Microscope Image Contrast for Thin Crystal, *Zeitschrift für Naturforschung A* 27 (3) (1972) 445–451, publisher: De Gruyter Section: Zeitschrift für Naturforschung A. doi:10.1515/zna-1972-0312.
URL <https://www.degruyterbrill.com/document/doi/10.1515/zna-1972-0312/html>
- [71] J. Luczka, M. Niemiec, A master equation for quantum systems driven by Poisson white noise, *Journal of Physics A: Mathematical and General* 24 (17) (1991) L1021. doi:10.1088/0305-4470/24/17/010.
URL <https://dx.doi.org/10.1088/0305-4470/24/17/010>
- [72] T. Seki, Y. Ikuhara, N. Shibata, Theoretical framework of statistical noise in scanning transmission electron microscopy, *Ultramicroscopy* 193 (2018) 118–125. doi:10.1016/j.ultramic.2018.06.014.
URL <https://www.sciencedirect.com/science/article/pii/S0304399118300603>
- [73] U. Weierstall, Q. Chen, J. C. H. Spence, M. R. Howells, M. Isaacson, R. R. Panepucci, Image reconstruction from electron and X-ray diffraction patterns using iterative algorithms: experiment and simulation, *Ultramicroscopy* 90 (2) (2002) 171–195. doi:10.1016/S0304-3991(01)00134-6.
URL <https://www.sciencedirect.com/science/article/pii/S0304399101001346>
- [74] A. V. Martin, A. I. Bishop, D. M. Paganin, L. J. Allen, Practical implementation of a direct method for coherent diffractive imaging, *Ultramicroscopy* 111 (7) (2011) 777–781. doi:10.1016/j.ultramic.2010.10.003.
URL <https://www.sciencedirect.com/science/article/pii/S0304399110002573>
- [75] A. Drenth, A. Huizer, H. Ferwerda, The Problem of Phase Retrieval in Light and Electron Microscopy of Strong Objects, *Optica Acta: International Journal of Optics* 22 (7) (1975) 615–628, publisher: Taylor & Francis eprint:

- <https://doi.org/10.1080/713819083>. doi:10.1080/713819083.
URL <https://doi.org/10.1080/713819083>
- [76] S. Li, N. Gauquelin, R. H. L. Lalandec, A. Annys, C. Gao, C. Hofer, T. J. Pennycook, J. Verbeeck, Improving the low-dose performance of aberration correction in single sideband ptychography doi:10.48550/arXiv.2505.09555.
URL <http://arxiv.org/abs/2505.09555>
- [77] H. Yang, P. Ercius, P. D. Nellist, C. Ophus, Enhanced phase contrast transfer using ptychography combined with a pre-specimen phase plate in a scanning transmission electron microscope, *Ultramicroscopy* 171 (2016) 117–125. doi:10.1016/j.ultramic.2016.09.002.
URL <https://www.sciencedirect.com/science/article/pii/S0304399116301966>
- [78] R. Gerchberg, W. Saxton, A Practical Algorithm for the Determination of Phase from Image and Diffraction Plane Pictures, *Optik* 35.
- [79] R. Gerchberg, Super-resolution through Error Energy Reduction, *Optica Acta: International Journal of Optics* 21 (9) (1974) 709–720, publisher: Taylor & Francis eprint: <https://doi.org/10.1080/713818946>. doi:10.1080/713818946.
URL <https://doi.org/10.1080/713818946>
- [80] O. Melnyk, On connections between Amplitude Flow and Error Reduction for phase retrieval and ptychography, *Sampling Theory, Signal Processing, and Data Analysis* 20 (2) (2022) 16. doi:10.1007/s43670-022-00035-5.
URL <https://doi.org/10.1007/s43670-022-00035-5>
- [81] M. Guizar-Sicairos, J. R. Fienup, Phase retrieval with transverse translation diversity: a nonlinear optimization approach, *Optics Express* 16 (10) (2008) 7264–7278, publisher: Optica Publishing Group. doi:10.1364/OE.16.007264.
URL <https://opg.optica.org/oe/abstract.cfm?uri=oe-16-10-7264>
- [82] M. Odstrčil, A. Menzel, M. Guizar-Sicairos, Iterative least-squares solver for generalized maximum-likelihood ptychography, *Optics Express* 26 (3) (2018) 3108–3123, publisher: Optica Publishing Group. doi:10.1364/OE.26.003108.
URL <https://opg.optica.org/oe/abstract.cfm?uri=oe-26-3-3108>
- [83] P. Thibault, M. Guizar-Sicairos, Maximum-likelihood refinement for coherent diffractive imaging, *New Journal of Physics* 14 (6) (2012) 063004, publisher: IOP Publishing. doi:10.1088/1367-2630/14/6/063004.
URL <https://dx.doi.org/10.1088/1367-2630/14/6/063004>
- [84] J. Madsen, T. Susi, The abTEM code: transmission electron microscopy from first principles, *Open Research Europe* 1 (2021) 24. doi:10.12688/openreseurope.13015.1.
URL <https://open-research-europe.ec.europa.eu/articles/1-24/v1>
- [85] H. Huang, B. Pradhan, J. Hofkens, M. B. J. Roeffaers, J. A. Steele, Solar-Driven Metal Halide Perovskite Photocatalysis: Design, Stability, and Performance, *ACS Energy Letters* 5 (4) (2020) 1107–1123, publisher: American Chemical Society. doi:10.1021/acsenergylett.0c00058.
URL <https://doi.org/10.1021/acsenergylett.0c00058>
- [86] A. Dey, J. Ye, A. De, E. Debroye, S. K. Ha, E. Bladt, A. S. Kshirsagar, Z. Wang, J. Yin, Y. Wang, L. N. Quan, F. Yan, M. Gao, X. Li, J. Shamsi, T. Debnath, M. Cao, M. A. Scheel, S. Kumar, J. A. Steele, M. Gerhard, L. Chouhan, K. Xu, X.-g. Wu, Y. Li, Y. Zhang, A. Dutta, C. Han, I. Vincon, A. L. Rogach, A. Nag, A. Samanta, B. A. Korgel, C.-J. Shih, D. R. Gamelin, D. H. Son, H. Zeng, H. Zhong, H. Sun, H. V. Demir, I. G. Scheblykin, I. Mora-Seró, J. K. Stolarczyk, J. Z. Zhang, J. Feldmann, J. Hofkens, J. M. Luther, J. Pérez-Prieto, L. Li, L. Manna, M. I. Bodnarchuk, M. V. Kovalenko, M. B. J. Roeffaers, N. Pradhan, O. F. Mohammed, O. M. Bakr, P. Yang, P. Müller-Buschbaum, P. V. Kamat, Q. Bao, Q. Zhang, R. Krahne, R. E. Galian, S. D. Stranks, S. Bals, V. Biju, W. A. Tisdale, Y. Yan, R. L. Z. Hoye, L. Polavarapu, State of the Art and Prospects for Halide Perovskite Nanocrystals, *ACS Nano* 15 (7) (2021) 10775–10981, publisher: American Chemical Society. doi:10.1021/acsnano.0c08903.
URL <https://doi.org/10.1021/acsnano.0c08903>
- [87] O. Bunk, M. Dierolf, S. Kynede, I. Johnson, O. Marti, F. Pfeiffer, Influence of the overlap parameter on the convergence of the ptychographical iterative engine, *Ultramicroscopy* 108 (5) (2008) 481–487. doi:10.1016/j.ultramic.2007.08.003.
URL <https://www.sciencedirect.com/science/article/pii/S0304399107001969>
- [88] J. M. Cowley, A. F. Moodie, The scattering of electrons by atoms and crystals. I. A new theoretical approach, *Acta Crystallographica* 10 (10) (1957) 609–619, publisher: International Union of Crystallography. doi:10.1107/S0365110X57002194.
URL <https://journals.iucr.org/q/issues/1957/10/00/a02113/>
- [89] P. Goodman, A. F. Moodie, Numerical evaluations of N-beam wave functions in electron scattering by the multi-slice method, *Acta Crystallographica Section A: Crystal Physics, Diffraction, Theoretical and General Crystallography* 30 (2) (1974) 280–290, publisher: International Union of Crystallography. doi:10.1107/S056773947400057X.
URL <https://journals.iucr.org/a/issues/1974/02/00/a10626/>
- [90] K. Ishizuka, N. Uyeda, A new theoretical and practical approach to the multislice method, *Acta Crystallographica Section A: Crystal Physics, Diffraction, Theoretical and General Crystallography* 33 (5) (1977) 740–749, publisher: International Union of Crystallography. doi:10.1107/S0567739477001879.
URL <https://journals.iucr.org/a/issues/1977/05/00/a14220/>
- [91] A. Andrew Maiden, Ptychography algorithms from Sheffield University, original-date: 2023-12-22T11:31:17Z (May 2025).
URL <https://github.com/andyMaiden/SheffieldPtycho>
- [92] PyPtychoSTEM / pyPtychoSTEM · GitLab (May 2024).
URL <https://gitlab.com/pyptychostem/pyptychostem>
- [93] C. Hofer, C. Gao, T. Chennit, B. Yuan, T. J. Pennycook, Phase offset method of ptychographic contrast reversal correction, *Ultramicroscopy* 258 (2024) 113922. doi:10.1016/j.ultramic.2024.113922.
URL <https://www.sciencedirect.com/science/article/pii/S0304399124000019>